



OPEN

## A multimodal X-ray spectroscopy investigation of uranium speciation in $\text{ThTi}_2\text{O}_6$ compounds with the brannerite structure

Malin C. Dixon Wilkins<sup>1,2</sup>, Luke T. Townsend<sup>1</sup>, Martin C. Stennett<sup>1</sup>, Kristina O. Kvashnina<sup>3,4</sup>, Claire L. Corkhill<sup>1,5</sup>✉ & Neil C. Hyatt<sup>1,2,5</sup>

$\text{ThTi}_2\text{O}_6$  derived compounds with the brannerite structure were designed, synthesised, and characterised with the aim of stabilising incorporation of  $\text{U}^{5+}$  or  $\text{U}^{6+}$ , at dilute concentration. Appropriate charge compensation was targeted by co-substitution of  $\text{Gd}^{3+}$ ,  $\text{Ca}^{2+}$ ,  $\text{Al}^{3+}$ , or  $\text{Cr}^{3+}$ , on the Th or Ti site.  $\text{U L}_3$  edge X-ray Absorption Near Edge Spectroscopy (XANES) and High Energy Resolution Fluorescence Detected  $\text{U M}_4$  edge XANES evidenced  $\text{U}^{5+}$  as the major oxidation state in all compounds, with a minor fraction of  $\text{U}^{6+}$  (2–13%). The balance of X-ray and Raman spectroscopy data support uranate, rather than uranyl, as the dominant  $\text{U}^{6+}$  speciation in the reported brannerites. It is considered that the  $\text{U}^{6+}$  concentration was limited by unfavourable electrostatic repulsion arising from substitution in the octahedral Th or Ti sites, which share two or three edges, respectively, with neighbouring polyhedra in the brannerite structure.

The mineral brannerite, prototypically  $\text{UTi}_2\text{O}_6$ <sup>1</sup>, is of economic importance in production of uranium for the nuclear fuel cycle<sup>2</sup>. Although typically metamict due to self-radiation damage, natural brannerite specimens retain significant fractions of their actinide inventory under geochemical conditions over geological time-scales ( $10^7$ – $10^8$  Ma)<sup>3–6</sup>. Indeed, brannerite is known to be amongst the most refractory of uranium minerals, highly resistant to leaching under acidic conditions, but potentially less resistant to dissolution under alkaline conditions<sup>7,8</sup>. Consequently,  $\text{UTi}_2\text{O}_6$  is of interest as a host phase for the immobilisation of long lived actinides, such as plutonium, in tailored ceramic and glass–ceramic composite materials, as radioactive wasteforms<sup>9–21</sup>.

Taking the general formula  $\text{AB}_2\text{O}_6$ , the monoclinic brannerite structure, characteristic of  $\text{UTi}_2\text{O}_6$ , comprises corrugated sheets of edge sharing  $\text{BO}_6$  octahedra connected by chains of edge sharing  $\text{AO}_6$  octahedra, in space group  $\text{C2}/m^2$ . This structure is also adopted by the high temperature polymorph of  $\text{ThTi}_2\text{O}_6$ , synonymous with the mineral species thorutite<sup>22</sup>. Several  $\text{U}^{5+}$  dominant brannerites have been previously reported, typically stabilised by substitution of trivalent lanthanides on the U site (*i.e.*  $(\text{U}^{5+}_{0.5}\text{Ln}^{3+}_{0.5})\text{Ti}_2\text{O}_6$ ,  $\text{Ln}^{3+}$  including  $\text{Gd}^{3+}$ ,  $\text{Ce}^{3+}$ ,  $\text{Dy}^{3+}$ ,  $\text{Tb}^{3+}$ , etc.)<sup>9–14</sup>. Recently, we reported a novel  $\text{U}^{5+}$  dominant brannerite,  $\text{U}_{1.09}(\text{Ti}_{1.29}\text{Al}_{0.71})\text{O}_6$ , stabilised by an alternative crystal chemical strategy, involving  $\text{Al}^{3+}$  substitution on the Ti site<sup>17</sup>. Whilst the stability of  $\text{U}^{4+}$  and  $\text{U}^{5+}$  species within the brannerite structure is well-established, the stability of  $\text{U}^{6+}$  species is less clear, but evidently important to fully understand the geochemical stability of brannerite minerals, and the design and performance of their synthetic wasteform counterparts.

Previous investigation by Zhang et al. examined the compounds  $(\text{Th}_{0.85}\text{U}_{0.10}\text{Ca}_{0.05})\text{Ti}_2\text{O}_6$  (targeting  $\text{U}^{5+}$  only) and  $(\text{Th}_{0.90}\text{U}_{0.05}\text{Ca}_{0.05})\text{Ti}_2\text{O}_6$  (targeting  $\text{U}^{6+}$  only), based on  $\text{ThTi}_2\text{O}_6$ , with the brannerite structure<sup>15,16</sup>. The incorporation of uranyl species,  $(\text{UO}_2)^{2+}$ , was inferred based on the observation of weak bands at 780.9 and 807.8  $\text{cm}^{-1}$ , in the respective Raman spectra (attributed as the  $\nu_1$  symmetric stretch). However, no *direct determination* of uranium oxidation state, for example by X-ray absorption or photoelectron spectroscopy, was reported. Finnie et al. investigated  $(\text{Th}_{0.55}\text{U}_{0.30}\text{Ca}_{0.15})\text{Ti}_2\text{O}_6$ , and established  $\text{U}^{5+}$  as the dominant oxidation state (75%), with minor  $\text{U}^{4+}$  (15%) and  $\text{U}^{6+}$  (10%), using X-ray photoelectron spectroscopy (XPS)<sup>18</sup>. The  $\text{U}^{6+}$  contribution was considered to be a consequence of surface oxidation of the brannerite material, combined with the surface sensitivity

<sup>1</sup>Department of Materials Science and Engineering, University of Sheffield, Sheffield, UK. <sup>2</sup>School of Mechanical and Materials Engineering, Washington State University, Pullman, WA 99164, USA. <sup>3</sup>The Rossendorf Beamline at ESRF, CS 40220, 38043 Grenoble Cedex 9, France. <sup>4</sup>Institute of Resource Ecology, Helmholtz-Zentrum Dresden-Rossendorf, Bautzner Landstrasse 400, 01328 Dresden, Germany. <sup>5</sup>School of Earth Sciences, The University of Bristol, Bristol BS8 1RL, UK. ✉email: c.corkhill@sheffield.ac.uk

of XPS. Interestingly, a higher fraction of  $U^{4+}$  was determined from XPS data acquired from a polished surface of  $(Th_{0.55}U_{0.30}Ca_{0.15})Ti_2O_6$ , compared to a fracture surface, which was attributed to enrichment of  $Ca^{2+}$  and  $U^{5+}$  and/or  $U^{6+}$  at grain boundaries.

To further elucidate the incorporation and stability of  $U^{6+}$  in the brannerite structure, we designed three solid solutions based on  $ThTi_2O_6$ , targeting  $U^{5+}$  or  $U^{6+}$  speciation, with charge compensation by co-substitution on the Th or Ti site:

- $(Th_{0.85}U^{5+}_{0.10}Ca_{0.05})Ti_2O_6$  and  $(Th_{0.90}U^{6+}_{0.05}Ca_{0.05})Ti_2O_6$
- $(Th_{0.80}U^{5+}_{0.10}Gd_{0.10})Ti_2O_6$  and  $(Th_{0.85}U^{6+}_{0.05}Gd_{0.10})Ti_2O_6$
- $(Th_{0.95}U^{5+}_{0.05})(Ti_{1.95}M_{0.05})O_6$  and  $(Th_{0.95}U^{6+}_{0.05})(Ti_{1.90}M_{0.10})O_6$ ; with  $M^{3+} = Al^{3+}, Cr^{3+}$

Two additional compositions were also examined, reflecting the substitution of U for Th in the same proportions as the above compositions, without charge compensating species:

- $(Th_{0.95}U_{0.05})Ti_2O_6$  and  $(Th_{0.90}U_{0.10})Ti_2O_6$

Recognising that  $ThTi_2O_6$  does not present redox flexibility when prepared under oxidising conditions, our intent was to control uranium speciation as the most significant variable in each solid solution, by judicious co-substitution of appropriate charge compensating species with known oxidation state. Charge compensating species were chosen based on their previously reported solid solubilities in the brannerite structure and/or similar titanate structures:  $Ca^{2+}$  and  $Gd^{3+}$  on the  $Th^{4+}$  site<sup>9–11</sup>,  $Al^{3+}$  and  $Cr^{3+}$  on the  $Ti^{4+}$  site<sup>19,23,24</sup>. Note that compositions  $(Th_{0.85}U^{5+}_{0.10}Ca_{0.05})Ti_2O_6$  and  $(Th_{0.90}U^{6+}_{0.05}Ca_{0.05})Ti_2O_6$  are nominally identical to those previously investigated by Zhang et al., enabling a direct comparison, in principal, with this earlier study<sup>16</sup>.

Herein, we show that a minor fraction of  $U^{6+}$  (2–13%) was indeed stabilised within the synthesised brannerite compositions, by High Energy Resolution Fluorescence Detected (HERFD) X-ray Absorption Near Edge Spectroscopy (XANES) at the U  $M_4$  edge. However, both U  $L_3$  edge XANES and HERFD U  $M_4$  edge XANES evidenced  $U^{5+}$  as the major oxidation state in all compounds. The evidence in support of uranate and uranyl speciation, and the factors limiting the concentration of  $U^{6+}$ , are discussed.

## Results

**X-ray diffraction.** X-ray diffraction was used to characterise the phases present in each product, as shown in Fig. 1, and summarised in Table 1 and Table 2. A compound with the brannerite structure ( $ThTi_2O_6$ ; PDF #04-007-2825) was the major phase formed in all compositions. Trace quantities of  $TiO_2$  (rutile) and  $ThO_2$  were also present in many compositions; trace  $ThO_2$  was differentiated from  $UO_2$  by electron microscopy observation of the microstructure and EDX analysis. No reflections characteristic of  $UO_2$ ,  $U_3O_8$  or  $UO_3$  were observed; the estimated limit of detection of these oxides is around 0.5 wt% as determined by simulation of X-ray diffraction patterns. The diffraction patterns of compositions targeting  $Al^{3+}$  or  $Cr^{3+}$  substitution on the  $Ti^{4+}$  site, exhibited reflections characteristic of trace  $ThO_2$ . In contrast, the diffraction patterns of compositions targeting  $Ca^{2+}$  or  $Gd^{3+}$  substitution on the  $Th^{4+}$  site did not generally exhibit reflections characteristic of trace  $ThO_2$ .

**Unit cell parameters.** The unit cell parameters of synthesised brannerite phases were determined by LeBail analysis of XRD data (Table 1); the weighted average cation radii ( $r_w$ ) were estimated using appropriate Shannon radii (assuming as-batched compositions with U present as  $U^{5+}$  only)<sup>25</sup>. When compared to previously reported unit cell parameters for  $ThTi_2O_6$ <sup>26</sup>, the synthesised brannerites produced in this work had smaller overall unit cell volumes, in accordance with their reduced weighted average cation radii, as summarised in Table 2 and shown in Fig. 2 (e.g. 228.96(1) Å<sup>3</sup> for nominal composition  $(Th_{0.80}U_{0.10}Gd_{0.10})Ti_2O_6$  with  $r_w = 0.8506$  Å; compared to 231.21 Å<sup>3</sup> reported for  $ThTi_2O_6$  with  $r_w = 0.8567$  Å). The unit cell parameters  $b$  and  $c$ , and the angle  $\beta$ , generally decreased with the weighted average cation radii, as shown in Fig. 2; the change in the  $a$ -parameter was comparably small and hence a clear trend was not apparent. These observations are consistent with previous systematic studies of the response of the brannerite crystal structure to substitution on the U/Th and/or Ti sites<sup>13,21</sup>.

**U  $L_3$  edge XANES.** U  $L_3$  edge XANES data were acquired to assess the bulk U oxidation state. The position of the U  $L_3$  edge is dependent on the average U oxidation state, with some contribution from the local coordination environment of the U absorber. Initial examination of the acquired spectra, and U  $L_3$  edge position (see Fig. 3), suggested that  $U^{5+}$  was the dominant oxidation state in all materials (edge position determined by the energy position of the maximum in the first derivative). The presence of a high concentration of Th in all compositions examined, with the Th  $L_3$  edge at 16,300 eV, combined with the low U concentration (U  $L_3$  edge at 17,166 eV), resulted in very small edge steps and incomplete normalisation of monochromator glitches in the pre-edge regions.

Linear regression of the U  $L_3$  edge positions of the reference compounds ( $U^{4+}Ti_2O_6$ ,  $U^{5+}_{0.5}Yb_{0.5}Ti_2O_6$  and  $CaU^{6+}O_4$ ) was used to estimate the average bulk U oxidation state of the brannerite materials reported here. All estimated average U oxidation states were in the range 4.8(2) + to 5.1(2) +, as shown in Table 2. The highest U oxidation states were determined for  $(Th_{0.85}U_{0.05}Gd_{0.10})Ti_2O_6$ , with sufficient  $Gd^{3+}$  to charge balance 0.05 f.u.  $U^{6+}$  (6Gd), and  $(Th_{0.95}U_{0.05})(Ti_{1.90}Cr_{0.10})O_6$ , with sufficient  $Cr^{3+}$  to charge balance 0.05 f.u.  $U^{6+}$  (6Cr), both of which had estimated U oxidation states of 5.1(2) +.

As the individual contributions of  $U^{4+}$ ,  $U^{5+}$  and  $U^{6+}$  cannot be deconvoluted by conventional U  $L_3$  edge XANES, due to the core-hole lifetime broadening of the spectra, HERFD U  $M_4$  edge XANES spectra were also

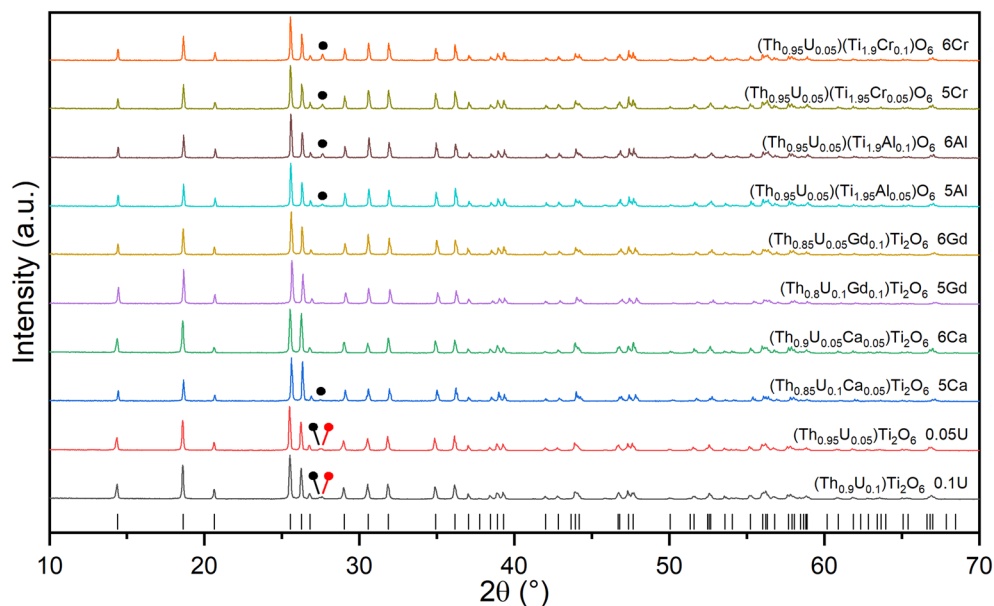


**Figure 1.** X-ray diffraction patterns of  $\text{ThTi}_2\text{O}_6$  compositions adopting the brannerite structure, targeting  $\text{U}^{5+}$  and  $\text{U}^{6+}$  incorporation with appropriate charge compensation; nominal compositions are summarized in Table 1 and Table 2. Tick marks below show the reflection positions of  $\text{ThTi}_2\text{O}_6$  (PDF #04-007-2825). Diagnostic reflections of  $\text{ThO}_2$  are marked with black circles;  $\text{TiO}_2$  (rutile) by red circles. Composition identifiers generally use the nomenclature  $nEl$ , where  $n$  is the target U oxidation state and  $El$  is the charge compensating element.

Nominal Composition	ID	a (Å)	b (Å)	c (Å)	$\beta$ (°)	Volume (Å <sup>3</sup> )	$R_{wp}$	GOF	$r_w$ (Å)
$(\text{Th}_{0.90}\text{U}_{0.10})\text{Ti}_2\text{O}_6$	0.1U	9.8133(3)	3.81475(8)	7.0226(2)	118.780(1)	230.420(10)	9.39	1.51	0.8506
$(\text{Th}_{0.95}\text{U}_{0.05})\text{Ti}_2\text{O}_6$	0.05U	9.8092(2)	3.81617(6)	7.0232(1)	118.786(1)	230.416(8)	9.77	1.57	0.8536
$(\text{Th}_{0.85}\text{U}_{0.10}\text{Ca}_{0.05})\text{Ti}_2\text{O}_6$	5Ca	9.8174(2)	3.80461(7)	7.0087(1)	118.775(1)	229.456(9)	12.88	1.20	0.8516
$(\text{Th}_{0.90}\text{U}_{0.05}\text{Ca}_{0.05})\text{Ti}_2\text{O}_6$	6Ca	9.8187(2)	3.81439(7)	7.0220(1)	118.801(1)	230.458(9)	13.60	1.20	0.8546
$(\text{Th}_{0.80}\text{U}_{0.10}\text{Gd}_{0.10})\text{Ti}_2\text{O}_6$	5Gd	9.8164(2)	3.79973(6)	7.0024(1)	118.765(1)	228.956(8)	9.66	1.07	0.8506
$(\text{Th}_{0.85}\text{U}_{0.05}\text{Gd}_{0.10})\text{Ti}_2\text{O}_6$	6Gd	9.8221(2)	3.80485(8)	7.0102(2)	118.789(1)	229.600(9)	11.32	1.08	0.8536
$(\text{Th}_{0.95}\text{U}_{0.05})(\text{Ti}_{1.95}\text{Al}_{0.05})\text{O}_6$	5Al	9.8114(2)	3.81346(6)	7.0170(1)	118.835(1)	229.988(7)	10.93	1.07	0.8525
$(\text{Th}_{0.95}\text{U}_{0.05})(\text{Ti}_{1.90}\text{Al}_{0.10})\text{O}_6$	6Al	9.8107(2)	3.81329(6)	7.0163(1)	118.834(1)	229.944(7)	10.65	1.07	0.8513
$(\text{Th}_{0.95}\text{U}_{0.05})(\text{Ti}_{1.95}\text{Cr}_{0.05})\text{O}_6$	5Cr	9.8163(2)	3.81668(7)	7.0220(1)	118.824(1)	230.487(8)	11.03	1.05	0.8538
$(\text{Th}_{0.95}\text{U}_{0.05})(\text{Ti}_{1.9}\text{Cr}_{0.10})\text{O}_6$	6Cr	9.8170(2)	3.81633(5)	7.0216(1)	118.837(1)	230.441(6)	10.40	1.07	0.8540
$\text{ThTi}_2\text{O}_6$	26	9.8140(2)	3.8228(1)	7.0313(2)	118.82(1)	231.12*	–	–	0.8567
$\text{UTi}_2\text{O}_6$	8	9.8123(15)	3.7697(6)	6.9253(9)	118.957(6)	224.14*	–	–	0.8400
$(\text{U}_{0.54}\text{Y}_{0.46})\text{Ti}_2\text{O}_6$	27	9.8039(2)	3.7188(1)	6.8403(2)	118.52(1)	219.12(1)	–	–	0.8241
$(\text{U}_{0.74}\text{Ca}_{0.26})\text{Ti}_2\text{O}_6$	11	9.8008(2)	3.7276(1)	6.8745(1)	118.38(1)	220.97(1)	–	–	0.8175
$(\text{U}_{0.50}\text{Tb}_{0.50})\text{Ti}_2\text{O}_6$	12	9.808(2)	3.725(4)	6.871(9)	118.51*	220.6(1)	–	–	0.8238
$(\text{U}_{0.50}\text{Dy}_{0.50})\text{Ti}_2\text{O}_6$	12	9.810(2)	3.723(4)	6.857(8)	118.49*	220.1(1)	–	–	0.8220
$(\text{U}_{0.49}\text{Y}_{0.51})\text{Ti}_2\text{O}_6$	13	9.8086(6)	3.7179(3)	6.8418(5)	118.52(6)	219.2(1)	–	–	0.8205

**Table 1.** Unit cell parameters determined from LeBail analysis of X-ray diffraction patterns for  $\text{ThTi}_2\text{O}_6$  compositions, adopting the brannerite structure, targeting  $\text{U}^{5+}$  and  $\text{U}^{6+}$  incorporation with appropriate charge compensation, together with selected literature data. A weighted average cation radius ( $r_w$ ) was calculated assuming nominal or reported compositions as appropriate, assuming  $\text{U}^{5+}$ .  $R_{wp}$  and  $\chi^2$  goodness-of-fit metrics from the Le Bail analysis are also included. Sample identification reference (ID) refers to Fig. 1 and generally uses the nomenclature  $nEl$ , where  $n$  is the target U oxidation state and  $El$  is the charge compensating element (or otherwise refers to a literature reference). \*Calculated from literature reports of the unit cell parameters.

acquired to ascertain, conclusively, the contributions of the different U oxidation states to the overall average speciation.

**HERFD U  $M_4$  edge XANES.** HERFD U  $M_4$  edge XANES allows for a more definitive determination of average U oxidation state due to greater relative separation between the edge positions of  $\text{U}^{4+}$ ,  $\text{U}^{5+}$  and  $\text{U}^{6+}$  and

Target brannerite composition	ID	Target U ox. State	Secondary phases	U ox. state L <sub>3</sub> edge LR	U ox. state M <sub>4</sub> edge LCF	U ox. state M <sub>4</sub> edge ITFA
(Th <sub>0.90</sub> U <sub>0.10</sub> )Ti <sub>2</sub> O <sub>6</sub>	0.1U	–	TiO <sub>2</sub> , ThO <sub>2</sub>	5.0(2)+	4.93(12)+	4.91(6)+
(Th <sub>0.95</sub> U <sub>0.05</sub> )Ti <sub>2</sub> O <sub>6</sub>	0.05U	–	TiO <sub>2</sub> , ThO <sub>2</sub>	5.0(2)+	4.91(12)+	4.89(6)+
(Th <sub>0.85</sub> U <sub>0.10</sub> Ca <sub>0.05</sub> )Ti <sub>2</sub> O <sub>6</sub>	5Ca	5+	ThO <sub>2</sub>	5.0(2)+	4.98(9)+	4.96(6)+
(Th <sub>0.90</sub> U <sub>0.05</sub> Ca <sub>0.05</sub> )Ti <sub>2</sub> O <sub>6</sub>	6Ca	6+	–	5.0(2)+	5.06(9)+	5.04(6)+
(Th <sub>0.80</sub> U <sub>0.10</sub> Gd <sub>0.10</sub> )Ti <sub>2</sub> O <sub>6</sub>	5Gd	5+	Trace TiO <sub>2</sub> /ThO <sub>2</sub>	4.9(2)+	5.06(7)+	5.04(6)+
(Th <sub>0.85</sub> U <sub>0.05</sub> Gd <sub>0.10</sub> )Ti <sub>2</sub> O <sub>6</sub>	6Gd	6+	Trace TiO <sub>2</sub>	5.1(2)+	5.12(11)+	5.11(6)+
(Th <sub>0.95</sub> U <sub>0.05</sub> )(Ti <sub>1.95</sub> Al <sub>0.05</sub> )O <sub>6</sub>	5Al	5+	ThO <sub>2</sub>	4.8(2)+	5.04(9)+	5.02(6)+
(Th <sub>0.95</sub> U <sub>0.05</sub> )(Ti <sub>1.90</sub> Al <sub>0.10</sub> )O <sub>6</sub>	6Al	6+	ThO <sub>2</sub>	4.8(2)+	5.10(13)+	5.09(6)+
(Th <sub>0.95</sub> U <sub>0.05</sub> )(Ti <sub>1.95</sub> Cr <sub>0.05</sub> )O <sub>6</sub>	5Cr	5+	ThO <sub>2</sub>	4.9(2)+	5.00(11)+	4.98(6)+
(Th <sub>0.95</sub> U <sub>0.05</sub> )(Ti <sub>1.90</sub> Cr <sub>0.10</sub> )O <sub>6</sub>	6Cr	6+	ThO <sub>2</sub>	5.1(2)+	5.04(10)+	5.02(6)+

**Table 2.** Tabulated information from characterisation of ThTi<sub>2</sub>O<sub>6</sub> compositions, adopting the brannerite structure, targeting U<sup>5+</sup> and U<sup>6+</sup> incorporation with appropriate charge compensation (see Table 1). The secondary phases identified in the X-ray diffraction patterns and U oxidation states, as-determined by linear regression (LR) of the U L<sub>3</sub> edge position, and linear combination fitting (LCF) and iterative target transformation factor analysis (ITFA) of HERFD U M<sub>4</sub> edge XANES spectra, are also included.

reduced core–hole lifetime broadening<sup>28</sup>. As with the U L<sub>3</sub> edge spectra discussed above, the low U and high Th concentrations, in the materials examined, resulted in low intensities of the HERFD U M<sub>4</sub> spectra. The spectra of U<sup>4+</sup>Ti<sub>2</sub>O<sub>6</sub>, CrU<sup>5+</sup>O<sub>4</sub> and CaU<sup>6+</sup>O<sub>4</sub> reference compounds were also acquired for comparison and to support further quantitative analyses. Consistent with analysis of U L<sub>3</sub> edge spectra, initial examinations of the HERFD U M<sub>4</sub> edge XANES supported an average oxidation state close to U<sup>5+</sup>, evidenced by the principle feature at *ca.* 3726 eV, as shown in Fig. 4. Inspection of the HERFD U M<sub>4</sub> edge XANES of (Th<sub>0.90</sub>U<sub>0.10</sub>)Ti<sub>2</sub>O<sub>6</sub> and (Th<sub>0.95</sub>U<sub>0.05</sub>)Ti<sub>2</sub>O<sub>6</sub>, also identified a small but distinct contribution at *ca.* 3725 eV, Fig. 4, demonstrating the presence of an additional minor component of U<sup>4+</sup>. Inspection of the HERFD U M<sub>4</sub> edge XANES of some compositions targeting U<sup>6+</sup>, most obviously (Th<sub>0.90</sub>U<sub>0.05</sub>Ca<sub>0.05</sub>)Ti<sub>2</sub>O<sub>6</sub> and (Th<sub>0.95</sub>U<sub>0.05</sub>)(Ti<sub>1.90</sub>Al<sub>0.10</sub>)O<sub>6</sub>, evidenced a small contribution at *ca.* 3727.5 eV, Fig. 4, attributed to the presence of U<sup>6+</sup><sup>28</sup>. The HERFD U M<sub>4</sub> edge XANES of materials with a uranyl speciation exhibit additional post-edge features, observed at *ca.* 3730 eV for CaU<sup>6+</sup>O<sub>4</sub>, see Fig. 4.<sup>28,29</sup> These features were not observed in any of the HERFD U M<sub>4</sub> spectra of the materials studied here, demonstrating that, although detectable fractions of U<sup>6+</sup> were present (see Table 2), uranate, rather than uranyl, is the dominant U<sup>6+</sup> speciation. Our confidence in this statement is tempered by the signal to noise ratio of the data and, certainly, a minor fraction of uranyl speciation cannot be conclusively ruled out.

Linear combination fitting (LCF) was utilised to estimate the proportions of U<sup>4+</sup>, U<sup>5+</sup>, and U<sup>6+</sup> and the average U oxidation state. Consistent with analysis of U L<sub>3</sub> edge spectra, LCF of the HERFD U M<sub>4</sub> edge spectra evidenced average U<sup>5+</sup> speciation, within the range 4.91(12) + to 5.12(12) + (detailed in Table 2). The compositions (Th<sub>0.90</sub>U<sub>0.10</sub>)Ti<sub>2</sub>O<sub>6</sub> and (Th<sub>0.95</sub>U<sub>0.05</sub>)Ti<sub>2</sub>O<sub>6</sub> were the least oxidised, with average U oxidation states of 4.93(12) + and 4.91(12) +, and U<sup>4+</sup> fractions of 14.9(20)% and 13.3(32)%, respectively. The most oxidised materials were: (Th<sub>0.85</sub>U<sub>0.05</sub>Gd<sub>0.10</sub>)Ti<sub>2</sub>O<sub>6</sub> and (Th<sub>0.95</sub>U<sub>0.05</sub>)(Ti<sub>1.90</sub>Al<sub>0.10</sub>)O<sub>6</sub>, with average U oxidation states of 5.12(11) + and 5.10(13) +, respectively. Fitting of the spectra of these compositions also necessitated a small but significant contribution from the U<sup>6+</sup> reference compound (CaU<sup>6+</sup>O<sub>4</sub>), of 14.6(11)% and 10.2(14)% respectively. These observations are in keeping with the oxidation states estimated from the U L<sub>3</sub> edge spectra, as well as previous reports of a fraction of retained U<sup>4+</sup> in air-synthesised charge compensated brannerites<sup>10,21</sup>.

Iterative Target Transformation Factor Analysis (ITFA) was also performed to evaluate the individual contributions of U<sup>4+</sup>, U<sup>5+</sup> and U<sup>6+</sup> to the final spectra and average U oxidation state. Initial principal component analysis of the brannerite and reference compounds determined that only three spectral-like components were necessary to reproduce all experimental spectra (see Supplementary Information, Fig. S1). This suggested that the spectra of the materials studied here can be well described by the three reference compounds.

Following the principal component analysis, the ITFA procedure was continued, with each of the three theoretical components accurately describing one of the reference compounds (see Supplementary Information, Fig. S1). As such, each component was assigned a given U oxidation state, with the relative fractions of each component utilised to calculate an average U oxidation state for the materials under examination. The relative fractions of the synthetic spectra and the calculated U oxidation states were both in excellent agreement with those calculated from linear combination fitting of the spectra (see Table 2; see Supplementary Information, Figs. S2–6).

This analysis was confirmed by repeating the ITFA procedure with a larger suite of U<sup>4+</sup>, U<sup>5+</sup> and U<sup>6+</sup> reference compounds, as well as only U<sup>4+</sup>Ti<sub>2</sub>O<sub>6</sub> and CaU<sup>6+</sup>O<sub>4</sub> reference compounds, to ensure the synthetic U<sup>5+</sup> spectrum was representative of the U<sup>5+</sup> contribution in these materials. In both cases the relative fractions of the synthetic spectra and overall U oxidation states were in very close agreement with both the linear combination fitting and the three reference compound ITFA.

The average U oxidation states determined by all methods (linear regression of the U L<sub>3</sub> edge position, and LCF and ITFA of the U M<sub>4</sub> edge) are in excellent agreement (see Table 2). The material shown to have the highest U oxidation state, (Th<sub>0.85</sub>U<sub>0.05</sub>Gd<sub>0.10</sub>)Ti<sub>2</sub>O<sub>6</sub>, contained 13.3(1)% U<sup>6+</sup> as determined by ITFA of the HERFD U M<sub>4</sub> edge spectrum (detailed in Supplementary Information Table S1). Assuming target stoichiometry, this

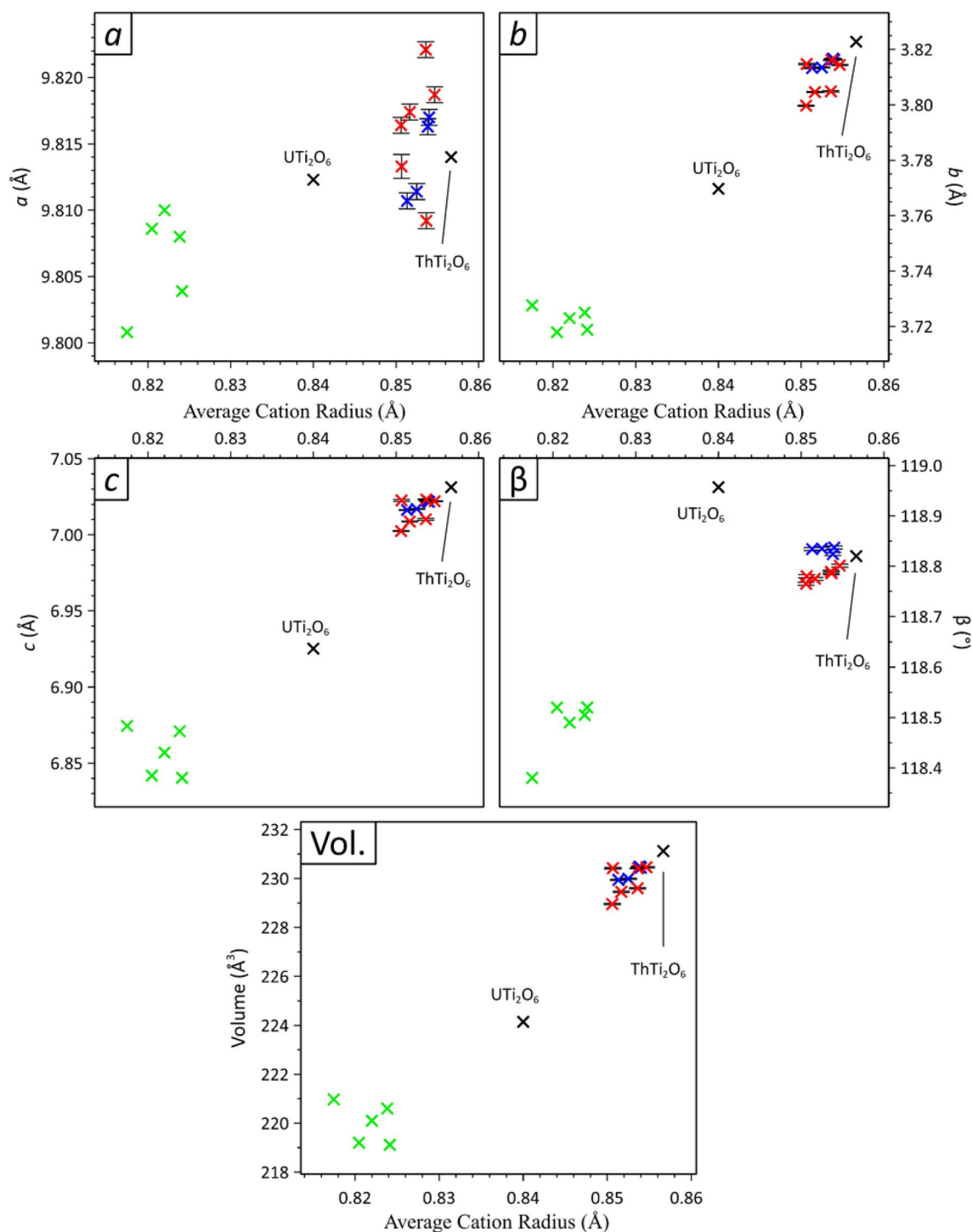


**Figure 2.** Plots of unit cell parameters, angle  $\beta$ , and volume, as a function of weighted average cation radius of compounds with the brannerite structure; data for  $\text{ThTi}_2\text{O}_6$  and  $\text{UTi}_2\text{O}_6$  are shown as black crosses; data from this study for  $\text{ThTi}_2\text{O}_6$  compositions targeting  $\text{U}^{3+}$  or  $\text{U}^{6+}$  incorporation, with appropriate charge compensation, are shown as red (Th site) and blue (Ti site) symbols; data for  $\text{U}^{5+}$  brannerites (derived from  $\text{UTi}_2\text{O}_6$ ) are shown as green symbols. See Table 1 for details.

corresponds to only 0.0133 f.u. of  $\text{U}^{6+}$ . No features relating to the presence of uranyl speciation were observed in the spectra of any of the materials produced here.

**Raman spectroscopy.** As expected from the near single phase nature of the materials produced here, determined by XRD, the Raman spectra of the brannerite compounds, Fig. 5, are in excellent agreement with previously reported spectra of actinide brannerites<sup>15,16</sup>. An earlier investigation of  $(\text{Th}_{0.85}\text{U}_{0.10}\text{Ca}_{0.05})\text{Ti}_2\text{O}_6$  and



( $\text{Th}_{0.90}\text{U}_{0.05}\text{Ca}_{0.05}$ ) $\text{Ti}_2\text{O}_6$  (i.e. the same nominal compositions as reported here) determined the presence of uranyl species, from analysis of Raman spectra. This assessment was made by assignment of the  $\nu_1$  symmetric stretch, apparent as a weak and broad band in the range 780–820  $\text{cm}^{-1}$ <sup>15</sup>, deconvoluted from the comparatively strong and intense band at 765–770  $\text{cm}^{-1}$  attributed to the  $A_g$  symmetric stretch of the  $\text{TiO}_6$  octahedra. The reported  $\nu_1$  stretch modes are within the wavenumber range previously determined for a diverse suite of uranyl compounds<sup>30,31</sup>. The  $\text{ThTi}_2\text{O}_6$  brannerite compounds investigated here all exhibited evidence of a weak and broad band, centred at 780  $\text{cm}^{-1}$ , apparent as a shoulder on the comparatively intense and sharp band, centred at 765  $\text{cm}^{-1}$ , which can confidently be assigned as the  $A_g$  symmetric stretch of  $\text{TiO}_6$  octahedra. However, we also observed the Raman spectrum of  $\text{ThTi}_2\text{O}_6$  to present such a shoulder on the  $A_g$  symmetric stretch of  $\text{TiO}_6$  octahedra at 765  $\text{cm}^{-1}$ , in agreement with earlier investigation<sup>15</sup>. It is evident that this band, also observed in the spectrum of  $\text{ThTi}_2\text{O}_6$ , must have at least some contribution from other Raman active modes of the brannerite structure (potentially arising from distortion of the  $\text{TiO}_6$  polyhedra). We believe caution should be exercised in attributing uranyl speciation in brannerite compounds by assignment of the weak and broad band deconvoluted at 780–820  $\text{cm}^{-1}$  as the  $\nu_1$  symmetric stretch. This is further evidenced by comparison of the Raman spectra of ( $\text{Th}_{0.85}\text{U}_{0.05}\text{Gd}_{0.10}$ ) $\text{Ti}_2\text{O}_6$  and ( $\text{Th}_{0.80}\text{U}_{0.10}\text{Gd}_{0.10}$ ) $\text{Ti}_2\text{O}_6$ . These compositions were determined to incorporate 13.3(1)% and 6.8(1)% of  $\text{U}^{6+}$  respectively (averaged from Table 1), but the weak and broad band centred at 780  $\text{cm}^{-1}$  is not strongly modulated, which is not consistent with a dominant uranyl speciation. We consider Raman spectroscopy to be inconclusive with regard to determination of uranyl speciation in the brannerite compounds reported here. If present, the concentration of uranyl species in the compounds examined in this work are very low, with even the most oxidised material containing only 0.0133 f.u. of  $\text{U}^{6+}$  as noted above. It should also be noted that as a result of the short excitation wavelengths utilised in standard Raman spectroscopy, it is a potentially surface sensitive technique with observations made from spectra not necessarily being representative of the bulk material, particularly in materials highly absorbing in the excitation laser regimes (532 nm) relevant to this work.

## Discussion

The aim of this study was to further investigate the stability of  $\text{U}^{6+}$  in the brannerite structure, in four  $\text{ThTi}_2\text{O}_6$  solid solutions, targeting  $\text{U}^{5+}$  or  $\text{U}^{6+}$  speciation, stabilised by co-substitution and charge compensation on the Th or Ti site. The materials studied here were produced to examine the possibility of stabilising a significant fraction of  $\text{U}^{6+}$  within the brannerite structure. HERFD  $\text{U } M_4$  edge spectra provided direct and unambiguous evidence for a small fraction of  $\text{U}^{6+}$  in all materials, however,  $\text{U}^{5+}$  was the major U oxidation state present (exceeding

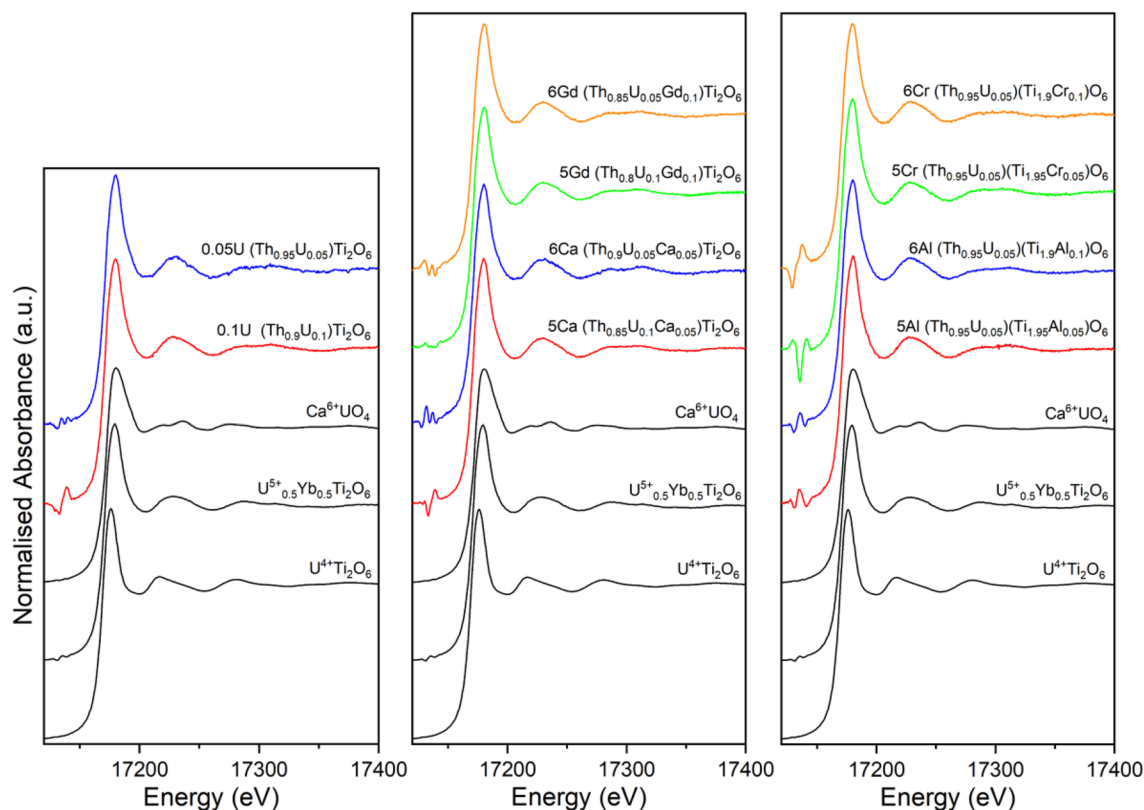


**Figure 3.**  $\text{U } L_3$  edge XANES spectra for  $\text{ThTi}_2\text{O}_6$  compositions, adopting the brannerite structure, targeting  $\text{U}^{5+}$  and  $\text{U}^{6+}$  incorporation with appropriate charge compensation (see Table 1). The spectra of  $\text{U}^{4+}\text{Ti}_2\text{O}_6$ ,  $\text{U}^{5+}_{0.5}\text{Yb}_{0.5}\text{Ti}_2\text{O}_6$  and  $\text{CaU}^{6+}\text{O}_4$  reference compounds are included for comparison. The corresponding average U oxidation states as-calculated by a linear regression are detailed in Table 2.

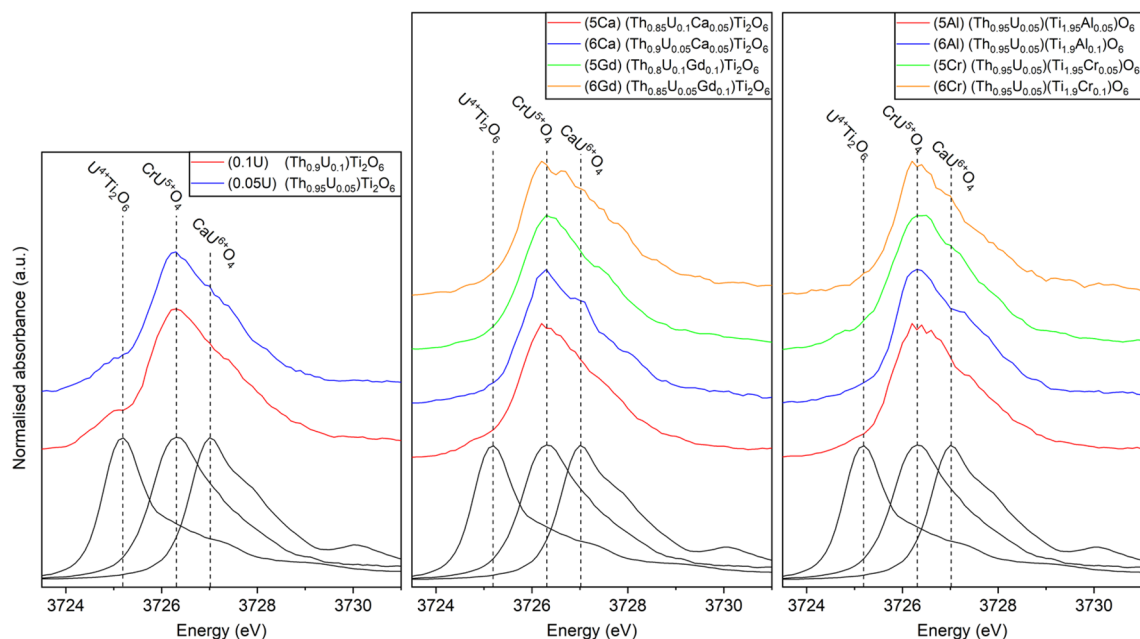


**Figure 4.** HERFD U  $M_4$  edge XANES of  $\text{ThTi}_2\text{O}_6$  compositions, adopting the brannerite structure, targeting  $\text{U}^{5+}$  and  $\text{U}^{6+}$  incorporation with appropriate charge compensation (see Table 1). The spectra of  $\text{U}^{4+}\text{Ti}_2\text{O}_6$ ,  $\text{CrU}^{5+}\text{O}_4$  and  $\text{CaU}^{6+}\text{O}_4$  reference compounds are included for comparison. The average U oxidation states determined from LCF and ITFA are detailed in Table 2.

77%, from ITFA).  $\text{U}^{5+}$  was dominant whether sufficient charge balancing species were present to permit oxidation of all U present to  $\text{U}^{6+}$  or not, or indeed when no charge balancing species were present (e.g.  $(\text{Th}_{0.90}\text{U}_{0.10})\text{Ti}_2\text{O}_6$ , 15.7(1)%  $\text{U}^{4+}$ , 77.3(6)%  $\text{U}^{5+}$ , 6.9(1)%  $\text{U}^{6+}$ , from ITFA). However, it is interesting to note that the average U oxidation states of materials targeting  $\text{U}^{6+}$  were generally characterised by a greater fraction of  $\text{U}^{6+}$  speciation, compared to those targeting  $\text{U}^{5+}$  speciation; for example,  $(\text{Th}_{0.85}\text{U}_{0.05}\text{Gd}_{0.10})\text{Ti}_2\text{O}_6$  and  $(\text{Th}_{0.80}\text{U}_{0.10}\text{Gd}_{0.10})\text{Ti}_2\text{O}_6$ , which were determined to incorporate 13.3(1)% and 6.8(1)%  $\text{U}^{6+}$  respectively from ITFA. Compositions designed to target  $\text{U}^{6+}$  speciation were determined to have a lower average oxidation state, closer to  $\text{U}^{5+}$ , which is likely to be realised by a low concentration of cation and/or oxygen vacancies, consistent with the detection of trace  $\text{ThO}_2$  and  $\text{TiO}_2$  impurities, and the known defect chemistry of the brannerite structure<sup>27,32,33</sup>. An earlier XPS study of  $(\text{Th}_{0.55}\text{U}_{0.30}\text{Ca}_{0.15})\text{Ti}_2\text{O}_6$ , with sufficient  $\text{Ca}^{2+}$  to charge balance  $\text{U}^{5+}$ , evidenced a higher contribution of  $\text{U}^{4+}$  to the U  $4f_{7/2}$  peak when collected on a polished surface, compared to an unpolished fracture surface<sup>10</sup>. This was attributed to apparent  $\text{Ca}^{2+}$  and  $\text{U}^{5+}$  and/or  $\text{U}^{6+}$  enrichment at the grain boundaries. Such enrichment of charge compensating elements in the grain boundaries of the materials studied here could also result in the determined bulk average oxidation state being lower than targeted, in addition to any cation and/or anion vacancies.

$\text{U L}_3$  edge and HERFD U  $M_4$  edge XANES are effectively bulk techniques, giving insight into the average U oxidation states and environments throughout a material. HERFD U  $M_4$  edge spectra provided direct and unambiguous evidence for a small fraction of  $\text{U}^{6+}$  in all materials, however, no features characteristic of uranyl speciation were observed, even in the most oxidised material,  $(\text{Th}_{0.85}\text{U}_{0.05}\text{Gd}_{0.10})\text{Ti}_2\text{O}_6$ , with 13.3(1)%  $\text{U}^{6+}$  from ITFA. Although Raman spectra evidenced a weak and broad band centred at  $780\text{ cm}^{-1}$ , potentially characteristic of a  $\nu_1$  symmetric stretch of uranyl species<sup>15,16</sup>, the evident presence of this band in the spectrum of  $\text{ThTi}_2\text{O}_6$  means that caution must be exercised in its diagnostic attribution to the presence of uranyl species in the brannerite structure. In comparison with X-ray spectroscopies, Raman spectroscopy using a 532 nm laser has a relatively low penetration depth in polycrystalline opaque materials such as those examined in this work, and may be more sensitive to uranyl speciation formed by surface oxidation. The data presented here directly and conclusively demonstrate the stabilisation of a small fraction of  $\text{U}^{6+}$  in the brannerite structure, but the balance of evidence tends to support uranate, rather than uranyl, as the dominant  $\text{U}^{6+}$  bulk speciation. Raman spectroscopy has proven more conclusive in substantiating the presence of uranyl speciation in metamict mineral brannerite, however, this may reflect past aqueous alteration of the specimen consistent with the observation of U-OH bending vibrations<sup>34</sup>.

A wide range of uranium (VI) oxometallates may be synthesised at high temperature in either air or oxygen atmosphere, so the partial pressure of oxygen is not thought to be the limiting factor in stabilisation of only a modest  $\text{U}^{6+}$  concentration in the  $\text{ThTi}_2\text{O}_6$  compounds reported here<sup>35</sup>. The unit cell volume and weighted average cation radius of these compounds were shown to be well within the actinide brannerite stability field, as shown by Fig. 2, which suggests that ionic size effects are also unlikely to be limiting of the  $\text{U}^{6+}$  concentration. The brannerite structure comprises corrugated sheets of  $\text{BO}_6$  octahedra, in which each  $\text{BO}_6$  octahedron shares three edges, with the sheets connected by chains of edge sharing  $\text{AO}_6$  octahedra, in which each  $\text{AO}_6$  octahedron shares two edges. In  $\text{ThTi}_2\text{O}_6$ , across the shared octahedral edges, the A...A cation distance is 3.823 Å, and the

B...B cation distances are 3.039 and 3.161 Å<sup>22</sup>. Substitution of U<sup>6+</sup> at either site would be expected to give rise to highly unfavourable electrostatic repulsions, as a consequence of the short approach distance to neighbouring cations, which we consider may be limiting on the concentration of U<sup>6+</sup> incorporation.

## Conclusions

ThTi<sub>2</sub>O<sub>6</sub> compounds with the brannerite structure were designed to incorporate U<sup>5+</sup> or U<sup>6+</sup>, at dilute concentration of 0.10 or 0.05 formula units, by appropriate charge compensation involving co-substitution of Gd<sup>3+</sup>, Ca<sup>2+</sup>, Al<sup>3+</sup>, or Cr<sup>3+</sup>. Near-single-phase compounds were produced in each case. X-ray absorption spectroscopies evidenced a majority U<sup>5+</sup> speciation in all compounds, regardless of the nature and relative fraction of the charge compensating species. All compositions exhibited a small contribution from a U<sup>6+</sup> oxidation state, as evidenced from HERFD U M<sub>4</sub> edge XANES, and in many cases also a small contribution of U<sup>4+</sup>. Compositions targeting only U<sup>6+</sup> were, in general, determined to contain a greater contribution of U<sup>6+</sup>. Although Raman spectra presented a weak and broad band plausibly indicative of uranyl speciation, the observation of this band from ThTi<sub>2</sub>O<sub>6</sub>, means that caution must be exercised in its diagnostic attribution to the presence of uranyl species in the brannerite structure. In contrast, no spectroscopic signatures of uranyl speciation were apparent in the HERFD U M<sub>4</sub> edge XANES, although the signal to noise ratio of the data presented here mean that a minor contribution of uranyl speciation cannot be ruled out. Therefore, the balance of our evidence tends to support uranate rather than uranyl, as the dominant U<sup>6+</sup> speciation in the brannerites reported here.

This investigation has demonstrated that the ThTi<sub>2</sub>O<sub>6</sub> brannerite structure can incorporate a small fraction of U<sup>6+</sup>, alongside a more significant inventory U<sup>5+</sup>, by charge compensation on the Th or Ti site. Stabilisation of U<sup>6+</sup> was not thought to be limited by the weighted average cation radii, which were within the stability field of the actinide brannerites, or conditions of synthesis, which were conducive to formation of U<sup>6+</sup> oxometallates. It is considered that the U<sup>6+</sup> concentration may be limited by unfavourable electrostatic repulsion arising from substitution in the octahedral Th or Ti sites, which share two or three edges, respectively, with neighbouring polyhedra in the brannerite structure.

## Methods

Materials were prepared by solid state reaction and sintering. Stoichiometric amounts (see Table 2) of UO<sub>2</sub>, ThO<sub>2</sub> (produced by decomposition of Th(NO<sub>3</sub>)<sub>4</sub>·5H<sub>2</sub>O at 550 °C), TiO<sub>2</sub> (anatase), CaTiO<sub>3</sub>, Gd<sub>2</sub>O<sub>3</sub>, Al<sub>2</sub>O<sub>3</sub>, and Cr<sub>2</sub>O<sub>3</sub> were homogenised by high energy ball milling (Fritsch Pulverisette 23 reciprocating ball mill, 30 Hz, 5 min) utilising yttria-stabilised zirconia mill pots and milling media, with isopropanol as a carrier fluid. The milled slurries were dried at 85 °C, and the resulting powder cakes broken up by hand in a mortar and pestle. The milled powders were then pressed into 10 mm pellets under 2 t (approx. 250 MPa). Pellets were heat treated in alumina crucibles at 1400 °C for 24 h in air.

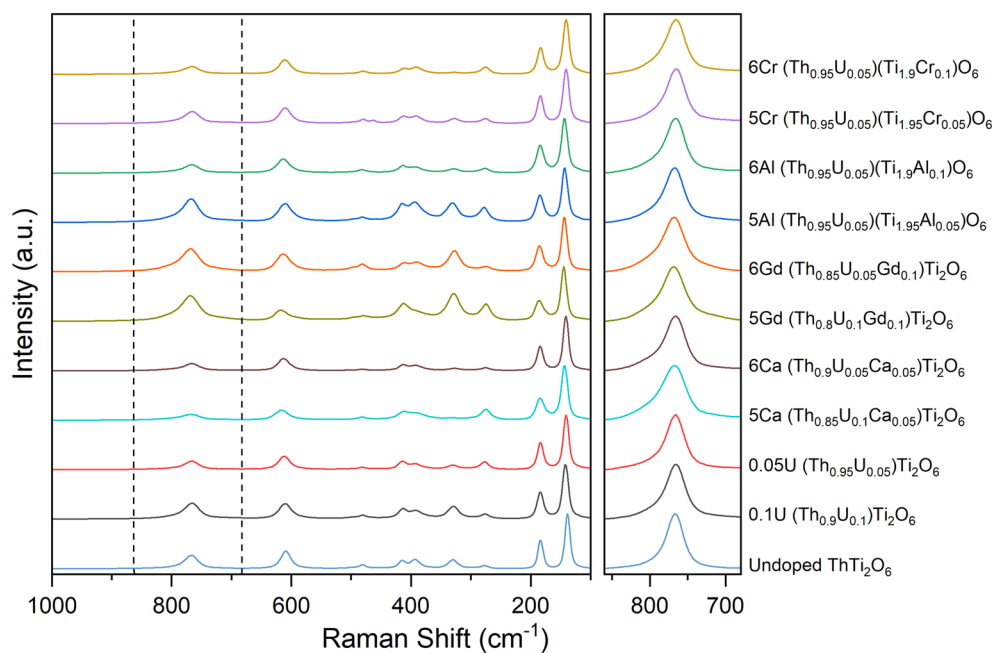


**Figure 5.** Normalised Raman spectra of ThTi<sub>2</sub>O<sub>6</sub> compositions, adopting the brannerite structure, targeting U<sup>5+</sup> and U<sup>6+</sup> incorporation with appropriate charge compensation (see Table 1). The panel shows of the region from 680 to 860 cm<sup>-1</sup>, showing a weak and broad band centred at 780 cm<sup>-1</sup> as an apparent as a shoulder on the comparatively intense and sharp band centred at 765 cm<sup>-1</sup>; the latter can confidently be assigned as the A<sub>g</sub> symmetric stretch of TiO<sub>6</sub> octahedra (spectra are normalized with respect to the intensity of the A<sub>g</sub> mode for comparison).



X-ray diffraction (XRD) patterns of each sample were collected on powdered material (Bruker D2 Phaser, Ni-filtered Cu K $\alpha$  radiation). Phase analysis was conducted by matching the reflections observed to phases in the PDF-4+ database<sup>36</sup>. Unit cell parameters of the brannerite phase in each composition were derived using LeBail method refinements, utilising the Topas<sup>37</sup> and JEdit<sup>38</sup> software packages. The background of each diffraction pattern was modelled with an eight term shifted Chebyshev polynomial; peak shapes resulting from instrumental and sample-based contributions were modelled using modified Thompson-Cox-Hastings (TCHZ) pseudo-Voigt functions.

Scanning electron microscopy with coupled energy dispersive X-ray spectroscopy (SEM/EDX) was used to confirm incorporation of the dopant cations. Due to the significant overlap between the Th M $\beta$  and U M $\alpha_1$  emissions, accurate compositional analysis was not possible. Solid samples were prepared for SEM/EDX analysis by mounting in a cold-set epoxy resin, polishing with increasingly fine grades of diamond suspensions, before coating with a conductive carbon layer. Backscattered electron micrographs and EDX spectra were collected using a Hitachi TM3030 (operating at 15 kV) microscope with Bruker Quantax 70 EDX system.

Raman spectra were collected on polished materials prior to carbon coating. Spectra at various points across the polished surfaces were collected using a Horiba XploRa PLUS Raman microscope with a 532 nm laser at 100 $\times$  magnification. The instrument was calibrated using the 520.7 cm $^{-1}$  band of a Si wafer.

U L $_3$  edge XANES were acquired at Diamond Light Source (DLS) beamline B18. The incident energy was selected using a Si (111) monochromator, with data collected in transmission mode from 16,970 to 17,560 eV. The intensities of the incident and transmitted beams were measured using ionisation chambers, operating in a stable region of their I/V curve. The K edge of an Y foil was used to calibrate the spectra, with the first peak in the first derivative of the Y foil spectrum set to 17,038 eV. The spectra of well-characterised specimens of UTi $_2$ O $_6$  (U $^{4+}$ , 6 coordinate), U $_{0.5}$ Yb $_{0.5}$ Ti $_2$ O $_6$  (U $^{5+}$ , 6 coordinate), and CaUO $_4$  (U $^{6+}$ , 8 coordinate) were collected to act as reference compounds of known U oxidation state. The energy position, E $_0$ , of each spectrum was determined by the energy position of the maximum in the first derivative.

High Energy Resolution Fluorescence Detected (HERFD) U M $_4$  edge XANES were collected at ESRF beamline BM20<sup>39</sup>. The incident energy was selected using the (111) reflection from a double Si crystal monochromator. XANES spectra were measured in HERFD mode using an X-ray emission spectrometer<sup>40</sup>. The sample, analyser crystal, and photon detector (Si drift detector) were arranged in a vertical Rowland geometry. HERFD U M $_4$  edge spectra were obtained by recording the maximum intensity of the U M $\beta$  emission line (ca. 3337 eV) as a function of the incident energy. The emission energy was selected using the (220) reflection of five spherically bent striped Si crystal analysers (1 m bending radius) aligned at a 75 $^\circ$  Bragg angle. The paths of the incident and emitted X-rays were minimised, and the sample was maintained under He atmosphere, in order to avoid losses in intensity due to absorption. Spectra of well-characterised specimens of UTi $_2$ O $_6$ , CrUO $_4$ , and CaUO $_4$  were also acquired to act as reference compounds of known U oxidation state (U $^{4+}$ , U $^{5+}$ , and U $^{6+}$  respectively).

Both U L $_3$  and HERFD U M $_4$  edge spectra were processed, and linear combination fitting of the U M $_4$  spectra performed, in Athena, part of the Demeter software package<sup>41,42</sup>. For Iterative Target Transformation Factor Analysis (ITFA), data were normalised using PyMca<sup>43</sup> and were analysed using the ITFA software package<sup>44,45</sup>, to further define the oxidation state of U within the samples<sup>20,46–48</sup>. Recent work has suggested that the errors on this analysis have not been fully quantified<sup>49,50</sup>, and therefore these values are considered to have a margin of error of 5%. Principal component analysis showed three components were generally necessary to describe the HERFD U M $_4$  edge spectra (those of the materials studied here plus U $^{4+}$ Ti $_2$ O $_6$ , Cr $^{5+}$ UO $_4$  and CaU $^{6+}$ O $_4$  reference compounds), and the initial fractions of the three components were set to unity for one of each of the reference compounds. The iterative target test procedure was then utilised to find the relative concentrations of the three components in the spectra of the materials studied here, with each component representing U $^{4+}$ , U $^{5+}$  or U $^{6+}$  according to comparisons with the reference compounds used. For validation, the procedure was then repeated twice, once including only U $^{4+}$ Ti $_2$ O $_6$ , CrU $^{5+}$ O $_4$  and CaU $^{6+}$ O $_4$  reference compounds and once including a wider range of reference compounds (CaU $^{6+}$ O $_4$ , SrU $^{6+}$ O $_4$ , U $^{6+}$ TiO $_5$ , CrU $^{5+}$ O $_4$ , U $^{5+}$ MoO $_5$ , U $^{4+}$ O $_2$  and U $^{4+}$ Ti $_2$ O $_6$ ). In both cases principal component analysis showed that three components were necessary to describe the spectra.

## Data availability

The datasets generated during and/or analysed during the current study are available from the corresponding author on reasonable request.

Received: 28 April 2023; Accepted: 17 July 2023

Published online: 07 August 2023

## References

- Hess, F. L. & Wells, R. C. Brannerite, a new uranium mineral. *J. Frankl. Inst.* **189**, 225–237. [https://doi.org/10.1016/S0016-0032\(20\)91588-0](https://doi.org/10.1016/S0016-0032(20)91588-0) (1920).
- Gilligan, R. & Nikoloski, A. N. The extraction of uranium from brannerite—A literature review. *Miner. Eng.* **71**, 34–48. <https://doi.org/10.1016/j.mineng.2014.10.007> (2015).
- Lumpkin, G. R., Leung, S. & Colella, M. Composition, geochemical alteration, and alpha-decay damage effects of natural brannerite. *Mat. Res. Symp. Proc.* **608**, 359–365. <https://doi.org/10.1557/PROC-608-359> (1999).
- Lumpkin, G. R. Alpha-decay damage and aqueous durability of actinide host phases in natural systems. *J. Nucl. Mater.* **289**, 136–166. [https://doi.org/10.1016/S0022-3115\(00\)00693-0](https://doi.org/10.1016/S0022-3115(00)00693-0) (2001).
- Zhang, Y. *et al.* Recrystallisation of amorphous natural brannerite through annealing: The effect of radiation damage on the chemical durability of brannerite. *J. Nucl. Mater.* **350**, 293–300. <https://doi.org/10.1016/j.jnucmat.2006.01.012> (2006).
- Lumpkin, G. R., Leung, S. H. F. & Ferenczy, J. Chemistry, microstructure, and alpha decay damage of natural brannerite. *Chem. Geol.* **291**, 55–68. <https://doi.org/10.1016/j.chemgeo.2011.09.008> (2012).

7. Ifill, R. O., Cooper, W. C. & Clark, A. H. Mineralogical and process controls on the oxidative acid-leaching of radioactive phases in Elliot Lake, Ontario, uranium ores: II: Brannerite and allied titaniferous assemblages. *CIM Bull.* **89**, 93–103 (1996).
8. Szymanski, J. T. & Scott, J. D. A crystal structure refinement of synthetic brannerite  $UTi_2O_6$  and its bearing on rate of alkaline-carbonate leaching of brannerite in ore. *Can. Mineral.* **20**, 271–280 (1982).
9. Vance, E. R., Watson, J. N., Carter, M. L., Day, R. A. & Begg, B. D. Crystal Chemistry and Stabilization in Air of Brannerite,  $UTi_2O_6$ . *J. Am. Ceram. Soc.* **84**, 141–144. <https://doi.org/10.1111/j.1151-2916.2001.tb00621.x> (2001).
10. Bailey, D. J., Stennett, M. C., Ravel, B., Grolmund, D. & Hyatt N. C. Synthesis and characterisation of brannerite compositions  $(U_{0.9}Ce_{0.1})_{1-x}M_xTi_2O_6$  ( $M = Gd^{3+}, Ca^{2+}$ ) for the immobilisation of MOX residues. *RSC Adv.* **8**, 2092–2099 (2018). <https://doi.org/10.1039/C7RA11742F>
11. James, M. & Watson, J. N. The synthesis and crystal structure of doped uranium brannerite phases  $U_{1-x}M_xTi_2O_6$  ( $M = Ca^{2+}, La^{3+}$ , and  $Gd^{3+}$ ). *J. Solid State Chem.* **165**, 261–265. <https://doi.org/10.1006/jssc.2002.9519> (2002).
12. Zhang, Y. *et al.* Uranium brannerite with Tb(III)/Dy(III) ions: Phase formation, structures, and crystallizations in glass. *J. Am. Ceram. Soc.* **102**, 7699–7709. <https://doi.org/10.1111/jace.16657> (2019).
13. Zhang, Y., Karatchevtseva, I., Kong, L., Wei, T. & Zhang, Z. Structural and spectroscopic investigations on the crystallization of uranium brannerite phases in glass. *J. Am. Ceram. Soc.* **101**, 5219–5228. <https://doi.org/10.1111/jace.15750> (2018).
14. Stefanovsky, S. V., Yudinsev, S. V., Shiryayev, A. A., Murzin, V. Y. & Trigub, A. L. Phase partitioning and uranium speciation in brannerite-based ceramics. *J. Eur. Ceram. Soc.* **37**, 771–777. <https://doi.org/10.1016/j.jeurceramsoc.2016.08.028> (2017).
15. Zhang, Y., Karatchevtseva, I., Qin, M., Middleburgh, S. C. & Lumpkin, G. R. Raman spectroscopic study of natural and synthetic brannerite. *J. Nucl. Mater.* **437**, 149–153. <https://doi.org/10.1016/j.jnucmat.2013.02.004> (2013).
16. Zhang, Y. *et al.* Theoretical and experimental Raman spectroscopic studies of synthetic thorutite ( $ThTi_2O_6$ ). *J. Nucl. Mater.* **446**, 68–72. <https://doi.org/10.1016/j.jnucmat.2013.11.037> (2014).
17. Zhang, Y., Gregg, D. J., Lumpkin, G. R., Begg, B. D. & Jovanovic, M. The incorporation of neptunium and plutonium in thorutite ( $ThTi_2O_6$ ). *J. Alloys Compd.* **581**, 665–670. <https://doi.org/10.1016/j.jallcom.2013.07.115> (2013).
18. Finnie, K. S., Zhang, Z., Vance, E. R. & Carter, M. L. Examination of U valence states in the brannerite structure by near-infrared diffuse reflectance and X-ray photoelectron spectroscopies. *J. Nucl. Mater.* **317**, 46–53. [https://doi.org/10.1016/S0022-3115\(03\)00004-7](https://doi.org/10.1016/S0022-3115(03)00004-7) (2003).
19. Dixon Wilkins, M. C. *et al.* Synthesis, characterization, and crystal structure of dominant uranium(V) brannerites in the  $UTi_{2-x}Al_xO_6$  system. *Inorg. Chem.* **60**, 18112–18121. <https://doi.org/10.1021/acs.inorgchem.1c02733> (2021).
20. Dixon Wilkins, M. C., Stennett, M. C. & Hyatt, N. C. The effect of A-site cation on the formation of brannerite ( $ATi_2O_6$ ,  $A = U, Th, Ce$ ) ceramic phases in a glass-ceramic composite system. *MRS Adv.* **5**, 73–81. <https://doi.org/10.1557/adv.2019.470> (2020).
21. Dixon Wilkins, M. C., Stennett, M. C., Maddrell, E. & Hyatt, N. C. The formation of stoichiometric uranium brannerite ( $UTi_2O_6$ ) glass-ceramic composites from the component oxides in a one-pot synthesis. *J. Nucl. Mater.* **542**, 152516. <https://doi.org/10.1016/j.jnucmat.2020.152516> (2020).
22. Ruh, R. & Wadsley, A. D. The crystal structure of  $ThTi_2O_6$  (brannerite). *Acta Crystallogr.* **21**, 974–978. <https://doi.org/10.1107/S0365110X66004274> (1966).
23. Vance, E. R. *et al.* Incorporation of uranium in zirconolite ( $CaZrTi_2O_7$ ). *J. Am. Ceram. Soc.* **85**, 1853–1859. <https://doi.org/10.1111/j.1151-2916.2002.tb00364.x> (2002).
24. Blackburn, L. R. *et al.* Synthesis and characterisation of  $Ca_{1-x}Ce_xZrTi_{2-2x}Cr_{2x}O_7$ : Analogue zirconolite wasteform for the immobilisation of stockpiled UK plutonium. *J. Eur. Ceram. Soc.* **40**, 5909–5919. <https://doi.org/10.1016/j.jeurceramsoc.2020.05.066> (2020).
25. Shannon, R. D. Revised effective ionic radii and systematic studies of interatomic distances in halides and chalcogenides. *Acta Cryst.* **A32**, 751–767. <https://doi.org/10.1107/S0567739476001551> (1976).
26. Mitchell, R. H. & Chakhmouradian, A. R. Solid solubility in the system  $NaLREE Ti_2O_6 - ThTi_2O_6$  (LREE, light rare-earth elements): Experimental and analytical data. *Phys. Chem. Miner.* **26**, 396–405. <https://doi.org/10.1007/s002690050200> (1999).
27. James, M., Carter, M. L. & Watson, J. N. The synthesis, crystal chemistry and structures of Y-doped brannerite ( $U_{1-x}Y_xTi_2O_6$ ) and thorutite ( $Th_{1-x}Y_xTi_2O_6$ ) phases. *J. Solid State Chem.* **174**, 329–333. [https://doi.org/10.1016/S0022-4596\(03\)00230-5](https://doi.org/10.1016/S0022-4596(03)00230-5) (2003).
28. Kvashnina, K. O. & Butorin, S. M. High-energy resolution X-ray spectroscopy at actinide  $M_{4,5}$  and ligand K edges: What we know, what we want to know, and what we can know. *Chem. Commun.* **58**, 327–342. <https://doi.org/10.1039/D1CC04851A> (2022).
29. Amidani, L. *et al.* Probing the local coordination of hexavalent uranium and the splitting of 5f orbitals induced by chemical bonding. *Inorg. Chem.* **60**, 16286–16293. <https://doi.org/10.1021/acs.inorgchem.1c02107> (2021).
30. Lu, G., Haes, A. J. & Forbes, T. Z. Detection and identification of solids, surfaces, and solutions of uranium using vibrational spectroscopy. *Coord. Chem. Rev.* **374**, 314–344. <https://doi.org/10.1016/j.ccr.2018.07.010> (2018).
31. Bartlett, J. R. & Cooney, R. P. On the determination of uranium–oxygen bond lengths in dioxouranium(VI) compounds by Raman spectroscopy. *J. Mol. Struct.* **193**, 295–300. [https://doi.org/10.1016/0022-2860\(89\)80140-1](https://doi.org/10.1016/0022-2860(89)80140-1) (1989).
32. Stennett, M. C., Freeman, C. L., Gandy, A. S. & Hyatt N. C., Crystal structure and non-stoichiometry of cerium brannerite:  $Ce_{0.975}Ti_2O_{5.95}$ . *J. Solid State Chem.*, **192**, 172–178 (2012) <https://doi.org/10.1016/j.jssc.2012.03.057>
33. Dixon Wilkins, M. C., Maddrell, E. R., Stennett, M. C. & Hyatt, N. C. The Effect of Temperature on the Stability and Cerium Oxidation State of  $CeTi_2O_6$  in Inert and Oxidizing Atmospheres. *Inorg. Chem.*, **59**, 17364–17373 (2020). <https://doi.org/10.1021/acs.inorgchem.0c02681>
34. Frost, R. L. & Reddy, B. J. Raman spectroscopic study of the uranyl titanate mineral brannerite ( $U, Ca, Y, Ce$ ) $2(Ti, Fe)2O_6$ : effect of metamictisation. *J. Raman Spectrosc.* **42**, 691–695. <https://doi.org/10.1002/jrs.2747> (2011).
35. Grenthe, I., *et al.* Uranium. In: Morss, L. R., Edelstein, N. M. & Fuger, J. (eds) *The Chemistry of the Actinide and Transactinide Elements*. Springer, Dordrecht, (2006). [https://doi.org/10.1007/978-94-007-0211-0\\_5](https://doi.org/10.1007/978-94-007-0211-0_5)
36. Gates-Rector, S. & Blanton, T. The powder diffraction file: A quality materials characterization database. *Powder Diffr.* **34**, 352–360. <https://doi.org/10.1017/S0885715619000812> (2019).
37. Coelho, A. A. TOPAS and TOPAS-academic: An optimization program integrating computer algebra and crystallographic objects written in C++. *J. Appl. Crystallogr.* **51**, 1. <https://doi.org/10.1107/S1600576718000183> (2018).
38. Evans, J. Advanced input files & parametric quantitative analysis using Topas. *Mater. Sci. Forum* **651**, 1–9. <https://doi.org/10.4028/www.scientific.net/MSF.651.1> (2010).
39. Scheinost, A. C. *et al.* ROBL-II at ESRF: A synchrotron toolbox for actinide research. *J. Synchrotron Radiat.* **28**, 1. <https://doi.org/10.1107/S1600577520014265> (2021).
40. Kvashnina, K. O. & Scheinost, A. C. A Johann-type X-ray emission spectrometer at the Rossendorf beamline. *J. Synchrotron Radiat.* **23**, 836–841. <https://doi.org/10.1107/S1600577516004483> (2016).
41. Ravel, B. & Newville, M. ATHENA and ARTEMIS: Interactive graphical data analysis using IFEFFIT. *Phys. Scr.* **2005**, T115. <https://doi.org/10.1238/Physica.Topical.115a01007> (2005).
42. Ravel, B. & Newville, M. ATHENA, ARTEMIS, HEPHAESTUS: data analysis for X-ray absorption spectroscopy using IFEFFIT. *J. Synchrotron Radiat.* **12**, 537–541. <https://doi.org/10.1107/S0909049505012719> (2005).
43. Sole, V. A., Papillon, E., Cotte, M., Walter, P. & Susini, J. A multiplatform code for the analysis of energy-dispersive X-ray fluorescence spectra. *Spectrochim. Acta, Part B* **62**, 63–68 (2007).
44. Rossberg, A. *et al.* Identification of uranyl surface complexes on ferrihydrite: Advanced EXAFS data analysis and CD-MUSIC modeling. *Environ. Sci. Technol.* **43**, 1400–1406. <https://doi.org/10.1021/es801727w> (2009).

45. Rossberg, A., Reich, T. & Bernhard, G. Complexation of uranium(VI) with protocatechuic acid—application of iterative transformation factor analysis to EXAFS spectroscopy. *Anal. Bioanal. Chem.* **376**, 631–638. <https://doi.org/10.1007/s00216-003-1963-5> (2003).
46. Roberts, H. E. *et al.* Uranium(V) incorporation mechanisms and stability in Fe(II)/Fe(III) (oxyhydr)oxides. *Environ. Sci. Technol. Lett.* **4**, 421–426. <https://doi.org/10.1021/acs.estlett.7b00348> (2017).
47. Pidchenko. *et al.* Uranium redox transformations after U(VI) coprecipitation with magnetite nanoparticles. *Environ. Sci. Technol.* **51**, 2217–2225 (2017). <https://doi.org/10.1021/acs.est.6b04035>
48. Leinders, G., Bes, R., Kvashnina, K. O. & Verwerf, M. Local structure in U(IV) and U(V) environments: The case of U<sub>3</sub>O<sub>7</sub>. *Inorg. Chem.* **59**, 4576–4587. <https://doi.org/10.1021/acs.inorgchem.9b03702> (2020).
49. Vitova, T. *et al.* The role of the 5f valence orbitals of early actinides in chemical bonding. *Nat. Commun.* **8**, 16053. <https://doi.org/10.1038/ncomms16053> (2017).
50. Vitova, T. *et al.* Competitive reaction of neptunium(V) and uranium(VI) in potassium-sodium carbonate-rich aqueous media: Speciation study with a focus on high-resolution X-ray spectroscopy. *Inorg. Chem.* **59**, 8–22. <https://doi.org/10.1021/acs.inorgchem.9b02463> (2020).
51. Hyatt, N.C. *et al.* The HADES facility for high activity decommissioning engineering & science: part of the UK National Nuclear User Facility, *IOP Conf. Ser.: Mater. Sci. Eng.* **818**, 012022 (2020). <https://doi.org/10.1088/1757-899X/818/1/012022>

## Acknowledgements

MDW is grateful to the UK EPSRC and Nuclear Decommissioning Authority for providing studentship through an EPSRC iCASE award, and CLC acknowledges the UK EPSRC for funding through an Early Career Research Fellowship (EP/N017374/1). This research utilised the HADES/MIDAS facility at the University of Sheffield established with financial support from EPSRC and BEIS, under grant EP/T011424/1<sup>51</sup>. We acknowledge the European Synchrotron Radiation Facility for provision of synchrotron radiation facilities and would like to thank Tatiana Polyakova, Anastasiia Smirnova, and Jurij Galanzaw for assistance in using beamline BM20 for U M<sub>4</sub> edge HERFD XAS data collection. KOK acknowledges support from the European Research Council (ERC) under grant number 759696. We acknowledge Diamond Light Source for access to Beamline B18 under Proposal No. SP1724.

## Author contributions

C.D.W.: Investigation, formal analysis, writing – original draft, review and editing. L.T.T.: formal analysis, writing – original draft. M.C.S.: investigation, writing – original draft, review and editing. K.O.K.: Methodology, data curation, writing—review and editing. N.C.H.: Supervision, project administration, resources, funding acquisition, methodology, investigation, writing – original draft, review and editing. C.L.C.: Writing—review and editing.

## Competing interests

The authors declare no competing interests.

## Additional information

**Supplementary Information** The online version contains supplementary material available at <https://doi.org/10.1038/s41598-023-38912-1>.

**Correspondence** and requests for materials should be addressed to C.L.C.

**Reprints and permissions information** is available at [www.nature.com/reprints](http://www.nature.com/reprints).

**Publisher's note** Springer Nature remains neutral with regard to jurisdictional claims in published maps and institutional affiliations.



**Open Access** This article is licensed under a Creative Commons Attribution 4.0 International License, which permits use, sharing, adaptation, distribution and reproduction in any medium or format, as long as you give appropriate credit to the original author(s) and the source, provide a link to the Creative Commons licence, and indicate if changes were made. The images or other third party material in this article are included in the article's Creative Commons licence, unless indicated otherwise in a credit line to the material. If material is not included in the article's Creative Commons licence and your intended use is not permitted by statutory regulation or exceeds the permitted use, you will need to obtain permission directly from the copyright holder. To view a copy of this licence, visit <http://creativecommons.org/licenses/by/4.0/>.

© The Author(s) 2023